Multispectral Optoacoustic Tomography (MSOT) at 64, 128 and 256 channels

Authors:

Alexander Dima, Dipl. Ing.
Institute for Biological and Medical Imaging, Helmholtz Zentrum München

Neal C. Burton, BA, PhD
iThera Medical GmbH

Vasilis Ntziachristos, MS, PhD, Full Professor at the Technical University of Munich

- Institute for Biological and Medical Imaging
  Helmholtz Zentrum München
- Chair for Biological Imaging
  Dept. of Medicine and Dept. of Electrical Engineering and Information Technology
  Technical University of Munich

Abstract

Optoacoustic (photoacoustic) imaging has already showcased the capacity to offer high resolution small animal visualization in-vivo in a variety of cancer, cardiovascular or neuroimaging applications. In particular, Multispectral Optoacoustic Tomography (MSOT) has shown imaging along the spectral and the time dimensions enabling sensing of multiple molecules over time and more recently in real-time. Furthermore, cross-sectional imaging of at least 20mm diameter has been showcased *in-vivo* in animals and humans using 64-element curved transducers placed along a single curved line. Herein we investigated the imaging improvements gained by utilizing a larger number of detectors and inquired whether more detectors will result in measurable image quality improvements. For this reason we implemented MSOT using 64, 128 and 256 element transducers and imaged the same phantoms and animals under similar conditions. Further corroborated by numerical simulation analysis, our findings quantify the improvements in resolution and overall image quality for the increasing number of detectors used pointing to significant improvements in image quality for the 256 detector array, over 64 or 128 detectors.

Keywords: optoacoustics, tomography, imaging systems

1. Introduction

Non-invasive imaging has become an important modality in small-animal research by enabling longitudinal insights *in-vivo* and on the same animal. Radiological imaging systems adapted from clinical use are routinely employed to visualize anatomical (CT, MRI) and molecular (SPECT, PET) features [1, 2]. Optical imaging has also emerged as a valuable investigative method. In addition to the central role that optical microscopy plays in biological interrogation, bioluminescence and fluorescence epi-illumination planar imaging and fluorescence molecular tomography (FMT) [3] have been disseminated in the biological and drug discovery laboratory. A major limitation however of optical imaging has been the limited resolution achieved for penetration depths larger than 0.5-1mm due to the strong photon scattering by tissues. For this reason optoacoustic (photoacoustic) imaging methods are increasingly considered as they can improve the resolution and optical imaging accuracy achieved over conventional optical methods, when imaging through several millimeters to centimeters of tissue.

Optoacoustic imaging operates on the local thermoelastic expansion of tissue, following absorption of transient light intensity incident on the tissue [4]. The thermoelastic expansion generated by different tissue photoabsorbing molecules yields broad-band ultrasonic waves, which can be sensed by ultrasound detectors. Image formation then requires the placement of detectors at multiple locations around the tissue of investigation and the subsequent processing of the data collected and their mathematical inversion (tomography) in order to produce images of the magnitude and location of the various photoabsorbing molecules present in the tissue [5]. By illuminating tissue at multiple wavelengths and using spectral detection (unmixing) techniques, multispectral optoacoustic tomography can then resolve multiple intrinsic tissue constituents or extrinsically administered agents and nanoparticles [6, 7].

Several optoacoustic implementations have been shown to achieve small animal imaging in two (2D) and three (3D) dimensions. Systems have been implemented using single detectors which are scanned in one or more dimensions [8-10], one-dimensional linear, curved or circular detector arrays [11-14] or two-dimensional detector arrangements [15-17] that place detectors on planar or curved surfaces. A recently developed 3D real-time optoacoustic system using a two-dimensional curved detector with 256 elements [16] traded in-plane resolution in favor of parallel volumetric scanning. In order to achieve high resolution and 3D imaging, other 3D

systems operate by scanning the detectors employed to achieve higher spatial sampling of optoacoustic signals. A major challenge of 3D imaging in this case is the long acquisition times typically required to obtain high-quality datasets.

2D imaging implementations have therefore a significant advantage over 3D imaging systems. By using one-dimensional arrays they can concentrate the number of detectors available for achieving high in-plane resolution. Out-of-plane signals can then be rejected by utilizing acoustically focused detectors. In this mode, 2D systems have been shown to achieve video-rate imaging of tissue cross-sections at a single wavelength [18] or more recently at multiple wavelengths [19]. Video-rate imaging is important to ensure fast tissue interrogation, monitoring dynamic events and minimize motion artifacts that are present in scanning systems. It would be possible to develop systems based on two-dimensional arrays using a large number of detectors to allow for high-quality video-rate 3D imaging. However, such implementations are currently largely impractical as they would require thousands of detectors in order to achieve the same in-plane resolution as 2D imaging systems. Besides challenges associated with complexity and cost, a further challenge of 3D systems is that they require illumination of entire volumes, which reduces the signal to noise ratio available to each of the two-dimensional images produced from the volume. Instead, one-dimensional array systems operate by concentrating the light energy available around the circumference of the tissue slice imaged, so that sources of lower power and therefore cost, can be utilized.

We previously introduced a one-dimensional curved array system optimized for high throughput, small-animal full-body imaging [18] and highlighted several in-vivo applications in small animal imaging using this technology [6, 20-22]. A variant of the system was introduced as a handheld device imaging the carotids and various other vessels and human tissue parts in-vivo [23], also more recently demonstrating multi-spectral imaging at video rates using a high-rate fast wavelength tuning laser [19]. Despite the high resolution imaging performance achieved, most imaging studies were performed using a 64-element one-dimensional curved array. Here we wanted to gain insights into the improvement achieved with higher density detectors and whether doubling and quadrupling the number of elements would lead to observable and desirable imaging improvement. Therefore, we implemented MSOT using detector arrays with 64, 128 and 256 elements and compared their relative performance. Experimental comparisons included imaging the same phantoms and interrogating the resolution, effective region of interest, image quality and sensitivity achieved with the

different detectors. These findings were also corroborated by numerical simulations. Finally, to showcase achievable imaging performance, we present a comparative study performed *in-vivo* on the same healthy mouse measured by all three systems within a short amount of time. We conclude that significant improvements in image quality, region of interest and sensitivity are observed with an increasing number of detectors to justify the investment of utilizing denser arrays for MSOT.

2. Materials and methods

2.1 Acoustic detection

All three arrays employed in this study were custom-made cylindrically focused curved-arrays (Imasonic S.A., France) with varying geometrical properties, yet manufactured from the same piezocomposite material to cover the frequency band up to 7.5MHz with peak sensitivity at 5MHz. To facilitate a concise description for the remainder of this text, we introduce a nomenclature based on the number of elements per array: MSOT64 (64 elements), MSOT128 (128 elements) and MSOT256 (256 elements). Fig. 1 illustrates apertures and overall arrangements of the three systems (left column MSOT64, right column MSOT128/256) and defines the coordinate system, which we will refer to in the following.

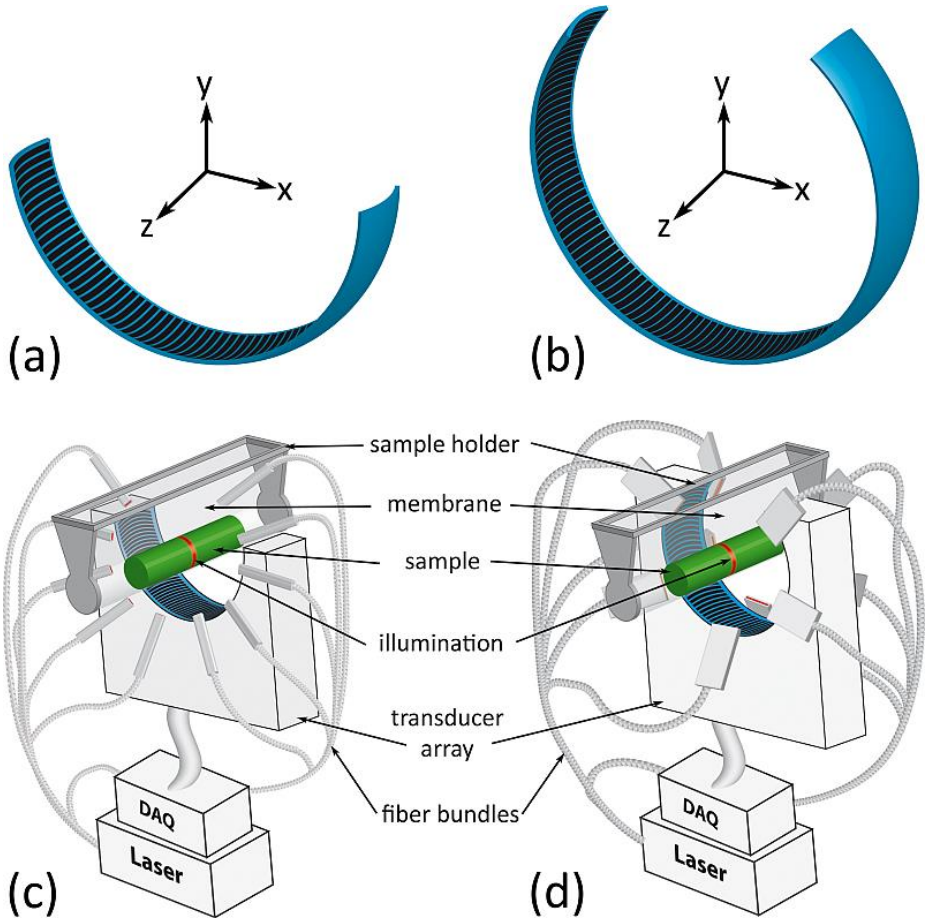

Fig. 1. The first row shows the transducer geometries for (a) MSOT64 and (b) MSOT128/MSOT256. The second row illustrates the two system setups including laser, data acquisition (DAQ) and sample holder with transparent membrane. (c) MSOT64 achieves even in-plane (z=0) illumination by using a ten arm fiber bundle arranged from one side at an angle of 33° relative to the circumference of the sample. (d) MSOT128/256 enables similar illumination by arranging a second ten arm fiber bundle symmetrically from both sides at an angle of 24°. Both fiber bundles cover an angle of 270° in the xy-plane.

The MSOT64 geometry is depicted in Fig. 1(a). This spherically concave array spans 172° in azimuth (xy-plane) and 10.8° in elevation (zy-plane) with a radius of 40mm. We define the origin of the coordinate system to coincide with the center of the hypothetical sphere described by the array such that the xy-plane at z=0 represents the imaging plane offering a cross-sectional view of the object. Translation along the z-axis thereby enables full-body imaging. Of the 64 elements making up the array each has a radius of 40mm, an azimuthal pitch of 1.88mm and a chord in elevation of 15mm (parallel to z-axis). At z=0 the extended length of the curvature in elevation constitutes

cylindrical focusing along the z-axis, while a comparably small pitch in azimuth allows a sufficient field of view (FOV) for tomographic imaging in the xy-plane. As the elements of all three arrays in this study are composed of the same piezocomposite material, but with varying geometrical sizes, we chose as the norm a single element of the MSOT64 and give it the area size and sensitivity of 100%. Both measures were determined by the manufacturer using standardized protocols and are thus comparable between arrays.

MSOT128, depicted in Fig. 1(b), covers a larger arc compared to MSOT64, spanning 270° in azimuth and 10.1° in elevation. This increase in azimuth coverage enables a more complete tomographic view, which is expected to significantly improve image quality. Together with the reduction of single element pitch to 1.47mm in azimuth, which increases the FOV of a single element, we also expect an improved transversal resolution, i.e. perpendicular to the radius. The resulting single element area size is only 72% of the MSOT64 norm and the sensitivity 55%. Nonetheless, due to twice the number of elements compared to MSOT64, the resulting full array sensitivity within areas of overlapping FOV should be 110%.

MSOT256 shares most of the geometrical characteristics with MSOT128, i.e. radius of 40mm, span in azimuth of 270° and 10.8° in elevation, and is also characterized by Fig. 1(b). However, the key difference lies in its number of elements (doubled again) and their geometry. A single element of MSOT256 is positioned on the array segment describing a sphere with radius 40mm, but is itself focused at 37mm radius, thus achieving toroidal focusing – as opposed to confocal focusing. Considering also the 270° azimuthal coverage including a reduced pitch of 0.735mm and the higher angular sampling by 256 elements, we expect yet more improvement in transversal resolution throughout a larger FOV. Even though the area size of a single element is merely 36% of the MSOT64 norm and corresponding sensitivity 29%, total sensitivity of the MSOT256 is expected to be 114% within overlapping FOV.

Using the geometrical characteristics of a single element we have numerically simulated the expected sensitivity field up to 7.5MHz in the imaging plane (z=0) for the single elements of each array – sensitivity being defined here as the maximum expected amplitude from a given position (x,y,0). By appropriately rotating and summing single element sensitivity fields we can obtain compound sensitivity fields for the three arrays employed (Fig. 2). The short solid lines marked by arrows and an element number on the images indicate the first and last element of the transducer. Black ellipses designate the region of full-width half-maximum (FWHM), i.e. where the amplitude drops to at most 50% of the peak value. For MSOT64, depicted in Fig. 2(a), the expected field is characterized by a diameter at FWHM of 15.5mm and a small displacement from the center of the array, due to the limited coverage of 172°. For MSOT128, shown in Fig. 2(b), calculations show a horizontal extent of 21mm and vertical extent of 17.1mm, due to the asymmetric distribution of detectors. The reduced pitch and toroidal focusing of MSOT256 elements result in a FWHM diameter of 32.6mm, shown in Fig. 2(c).

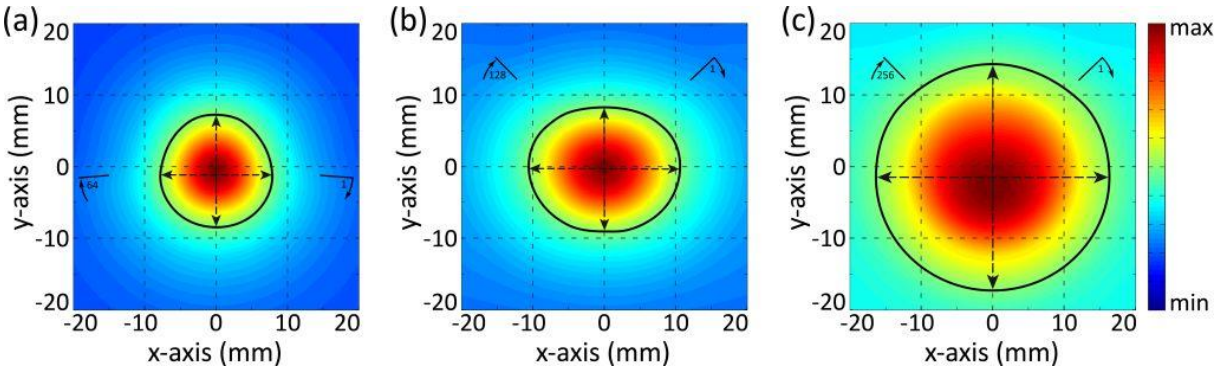

Fig. 2. Theoretical calculation of the 2D sensitivity field of detection (0.5-7.5 MHz) within the imaging plane of the detector. Black ellipses mark the full-width half-maximum (FWHM) range. The first and last element of each array is noted on the images by a short solid line marked with an arrow and element number. (a) 64 element array covering 172°; diameter at FWHM: 15.5 mm. (b) 128 element array covering 270°; vertical diameter at FWHM: 17.1 mm; horizontal diameter at FWHM: 21.0 mm. (c) 256 element array covering 270°; diameter at FWHM: 32.6 mm.

2.2 Experimental arrangement

The experimental arrangement utilized was comparable to a system previously described [18, 24]. Measurements employed a wavelength tunable pulsed laser (Phocus^{TM}, Opotek Inc., USA) with a pulse duration of <10ns, repetition rate of 10 Hz and peak pulse energy of 90 mJ at 750 nm. The laser beam was coupled into a ten arm fiber bundle. The MSOT64 system employed a bundle with rectangular outputs of size 3.2x0.72mm² at the distal end. The arms were arranged over an arc of 270° next to the detection array, as shown in Fig. 1(c), and established ring illumination at the imaging plane. The systems housing the MSOT128 and MSOT256 employed a slightly different illumination arrangement, depicted in Fig. 1(d). Ring illumination was implemented by five rectangular outputs of 12.4x0.2mm² size covering 270° in azimuth on both sides of the arrays. A custom made data acquisition (DAQ) system digitized up to 512 channels in parallel at 10 Hz repetition rate and 40 MSamples/s.

Image reconstruction was performed using a model-based algorithm [25]. The algorithm computes a model-matrix that links measured pressure values with a discrete grid of positions (image pixels) in the imaging plane by numerically evaluating the forward solution of the optoacoustic wave equation. Model inversion was achieved using a regularized iterative least-squares algorithm. All imaging results presented in this study were attained using the same set of parameters, i.e. 450x450 pixels over 30x30mm². Due to the large model-matrix and iterative inversion, reconstruction time per image necessitated offline reconstruction after the data acquisition.

2.3 Numerical simulation

To facilitate objective observations between the three detectors we employed numerical simulations. The simulations assumed a rectangular region of 30x30mm² centered at the origin in the

xy-plane (z=0) and placed 900 microspheres equally spaced by 1mm in x- and y-direction. Fig. 3(a) shows the numerical setup, which also represents the reconstruction target. To obtain acoustic data for the three arrays we first employed an ultrasound field simulation program (Field II [26, 27]) to compute the acoustic field received by each detection element following a Dirac-like excitation at the 900 microsphere positions. Then we convolved these geometric impulse responses, sampled at 40 MSamples/s, with the analytical optoacoustic signal emitted by a spherical absorber [28] and obtained acoustic data frames of size 2030x64, 2030x128 and 2030x256. Microsphere size was chosen to span six acoustic samples at 40MSamples/s, i.e. 125ns or 187.5μm at 1500 m/s speed of sound.

2.4 Phantoms

Known phantoms were also employed to provide for control measurements that could compare the performance of the three detectors employed. Validation of numerical results was achieved using black polyethylene (PE) microspheres of diameters ranging from 180-212 μm (Cospheric LLC, USA). Due to practical difficulties replicating the regular sampling grid used in the numerical simulation we decided to implement an irregularly sampled disk of 30 mm diameter. For this we prepared a cylindrical tissue mimicking agar (2%w/v) phantom of 50 mm height and 30 mm diameter including a fatty emulsion imparting a reduced scattering coefficient of $\mu_s'=10cm^{-1}$. We then dispersed microspheres on top of the phantom aiming to achieve an as even distribution as possible. The agar disk containing the microspheres was illuminated from one side through ~25mm of scattering agar using a cylindrical fiber bundle. Fluence variations within the disk were captured by a CCD camera at 680nm and these measurements were later employed for correction of the reconstructed image. Fig. 3(b) shows the acquired photograph from the back-illuminated disk.

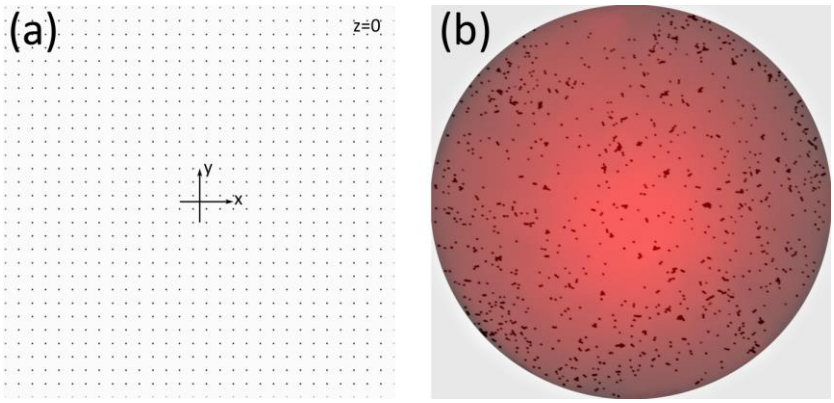

Fig. 3. (a) Numerical setup covering a rectangular region of 30x30mm² – 900 microspheres of 187.5µm diameter equally spaced in 1mm steps. (b) Top view photograph of the microsphere-containing phantom showing the sphere distribution and the fluence distribution. The disk diameter was 30 mm; the PE spheres attained diameters of 180-212µm.

2.5 Mouse imaging *in-vivo*

To extend numerical and phantom findings to tissue observations we imaged an eight-week-old female CD-1® Nude mouse *in-vivo* (Charles River Laboratories, Germany). Animal handling was conducted in compliance with protocols approved by the Bavarian Animal Research Authority. The animal was anesthetized using 1.8% Isoflurane (Forene©, Abbott AG, Switzerland) vaporized in 100% oxygen at 0.8L/min and subsequently placed within an animal holder, as described in [24], in a supine position relative to the arrays. The holder, designed to fit into all three systems, ensured identical positioning of the animal in relation to the detector for the three experimental arrangements. The imaging protocol involved a single-wavelength full-body scan with a step size of 0.5 mm. At each step we recorded 50 frames to capture periodically occurring motion induced by heart beat or breathing. This imaging sequence was repeated for all three systems.

3. Results

3.1 Numerical simulation

Results obtained from numerical simulation are shown in Figure 4. Fig. 4(a) corresponds to the reconstruction obtained from MSOT64, Fig. 4(b) from MSOT128 and Fig. 4(c) from MSOT256. All images were normalized to 1 and negative values were dismissed as they have no physical meaning. Two rectangular regions (4x4mm²) from the center and the periphery of each array are shown magnified at the bottom of each of the images they were taken from. The images demonstrate two major differences. First, a broader region of the object is visualized for an increasing number of elements employed, as predicted by the sensitivity fields of Fig. 2. The second difference regards the transversal resolution, i.e. the resolution perpendicular to radial lines originating in the middle of the image. Close to the array center all systems reconstruct the simulated microspheres with a similar performance and accuracy in obtaining their actual dimensions as shown at the bottom right magnification insets in Fig. 4(a-c). However, the further from the image center a microsphere is positioned the more its reconstruction is transversally elongated. The strength of this effect is directly related to the pitch of the detector elements in each array, i.e. MSOT64 elements have the largest pitch and cause the strongest distortions; MSOT256 elements the smallest pitch and the least distortions. The bottom left magnification insets in Fig. 4(a-c) illustrate this effect.

A quantitative assessment of both improvements seen as a function of detector elements employed is given in Fig. 4(d) and 4(e), which show a profile (cross-section) of the six magnified images from top-left to bottom-right. Close to the image center, Fig. 4(e), all geometries correctly resolve a microsphere diameter of 190µm at FWHM with comparable sensitivity (amplitude). The noise appearing between the four distinct peaks is a consequence of the high resolution and large imaging region chosen (30x30mm²), which required a degree of regularization inversely proportional to the number of detectors, i.e. stronger for MSOT64 than for MSOT256. On the other hand, transversal resolution at 10mm distance from the array center, shown in Fig. 4(d), drops for all systems. MSOT64 resolves elongated microspheres of approximately 730µm length; MSOT128 achieves 450µm and MSOT256 270µm for an actual microsphere size of 187.5µm. On the radial axis

all systems resolve microsphere width as approx. 250 µm. Fig. 4(d) and (e) also illustrate the drop in amplitude when moving further from the array center. While all systems exhibit reduced sensitivity with increasing distance from the center, the drop is sharpest for MSOT64 and marginally better for MSOT128. By contrast, MSOT256 achieves twice the sensitivity of MSOT64.

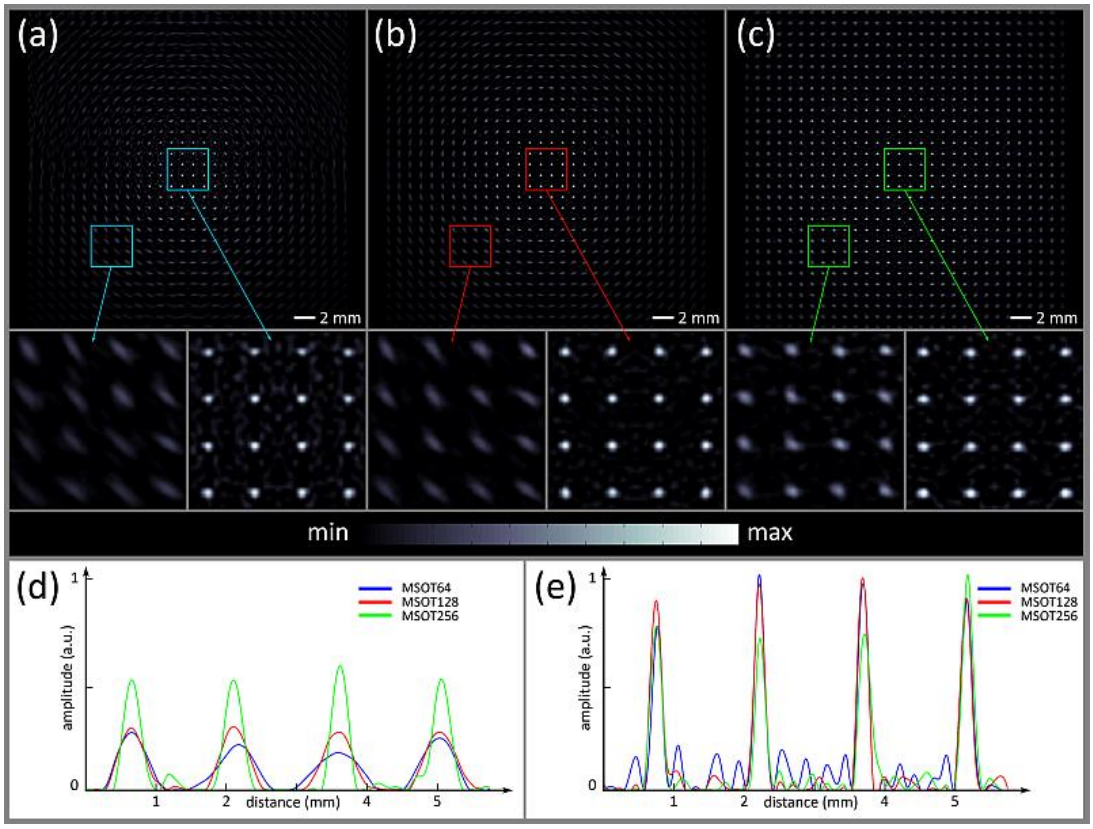

Fig. 4. Top row shows simulated reconstruction results from (a) MSOT64, (b) MSOT128 and (c) MSOT256. For each image negative values were removed and the remainder normalized to 1. Details at the periphery and the center, framed (4x4mm²) and color-coded by array, were magnified for display at the bottom left and right respectively. Graphs below depict diagonal cross-sections (top-left to bottom-right) of the magnified detail images for (d) the periphery and (e) the center.

3.2 Phantom measurements

Experimental results from the PE microsphere phantom are shown in Figure 5, which follows a figure arrangement similar to Fig. 4. Due to irregular sampling, we selected three central (4-6) and three

peripheral (1-3) microspheres, which were captured sufficiently well by all geometries, and plotted their transversal profiles in Fig. 5(d, e). We note that variations in amplitude and shape within close spatial proximity, e.g. within the magnification insets, are due to experimental imperfections such as microsphere clustering, see Fig. 3(b), alignment between phantom and array center or elevational displacement of individual microspheres (on the order of hundreds of µm along z-axis). Nonetheless, selected microspheres confirmed the observations derived from numerical simulation. In particular, microspheres 4-6 from the array center show similar shapes, amplitudes and resolutions for all systems. Fig. 5(e) plots profiles obtained along the diameter of the microspheres revealing a FWHM of ~200µm for all detectors employed. Conversely, selected microspheres (1-3) from the periphery were resolved with different diameters as a function of the number of detector elements employed, as shown in Fig. 5(d). We also observed higher sensitivity for MSOT128 compared to MSOT64 and the highest sensitivity for MSOT256. Similar observations can be made for transversal resolution in 10mm distance from the array center (microsphere 3): MSOT256 resolves a width of 200µm, MSOT128 300µm and MSOT64 450µm. In relative terms, i.e. from MSOT64 over MSOT128 to MSOT256, improvements in transversal resolution were expected; compared to simulation however, absolute resolutions seem too high. The explanation for this apparent outperformance of simulation results lies in the necessary light fluence correction and segmentation, which both are non-linear operations but consistent for all arrays. Considering the pixel size of 67µm/pixel, the transversal resolution discrepancy for MSOT256 is less than 1 pixel, for MSOT128 close to 2 pixels and for MSOT64 close to 4 pixels. Thus, experimental results from phantom confirm the superior image quality of MSOT256.

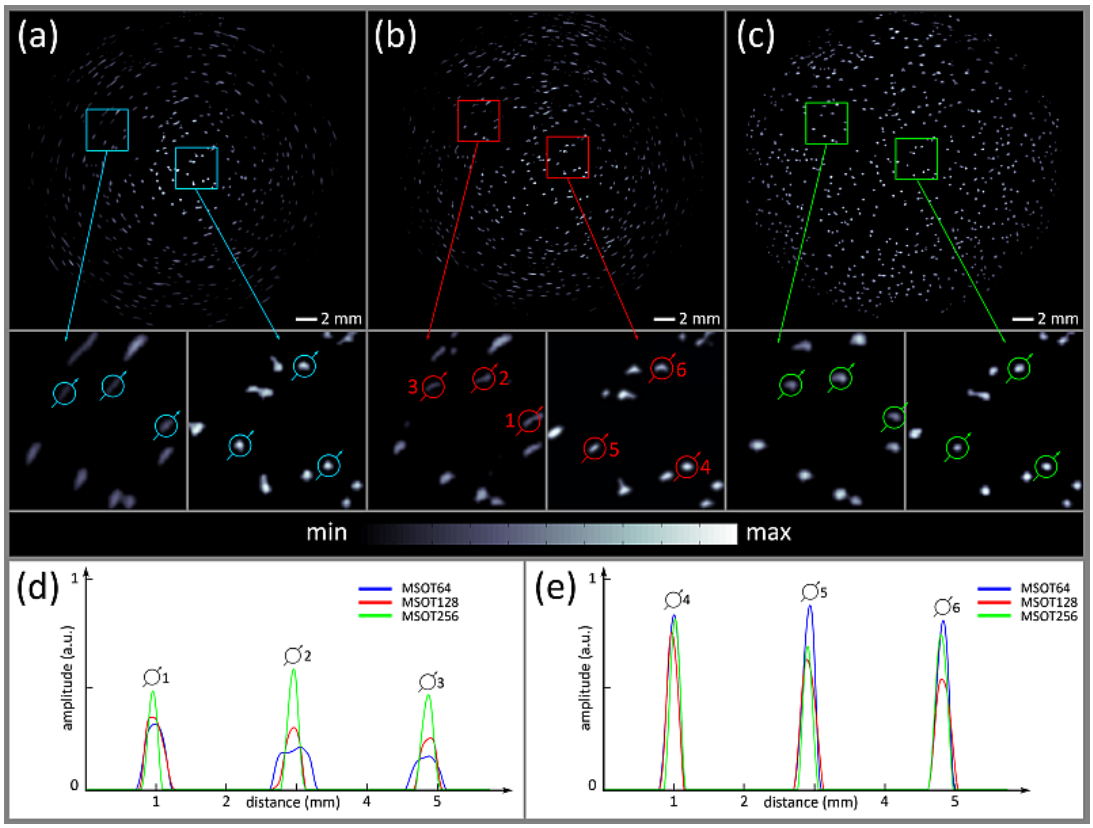

Fig. 5. Top row shows experimental phantom reconstruction results from (a) MSOT64, (b) MSOT128 and (c) MSOT256. For each image negative values were removed and the remainder normalized to 1. Furthermore, images were segmented based on their local maxima. Details at the periphery and the center, framed (4x4mm²) and color-coded by array, were magnified for display at the bottom left and right respectively. Graphs below depict diagonal cross-sections of individual microspheres (circled blue, red and green) for (d) the periphery (numbered 1-3) and (e) the center (numbered 4-6). Individual cross-sections were artificially spaced to allow sufficient distance for comparison.

3.3 Mouse imaging *in-vivo*

Figure 6 shows results obtained from the same nude mouse imaged sequentially and without averaging in all three systems. To qualitatively compare achievable imaging performance we have selected three content rich anatomical regions of increasing diameter. As the mouse was identically positioned during all three scans and we took 50 frames per position, we were able to precisely choose the same cross-sectional image at the same respiratory time point for all three systems. Thereby, results from MSOT64 are shown in the first column [Fig. 6(a),(e),(i)], from MSOT128 in the

second column [Fig. 6(b),(f),(j)] and from MSOT256 in the third column [Fig. 6(c),(g),(k)]. The last column [Fig. 6(d),(h),(l)] depicts cryoslices at equivalent positions from a comparable mouse.

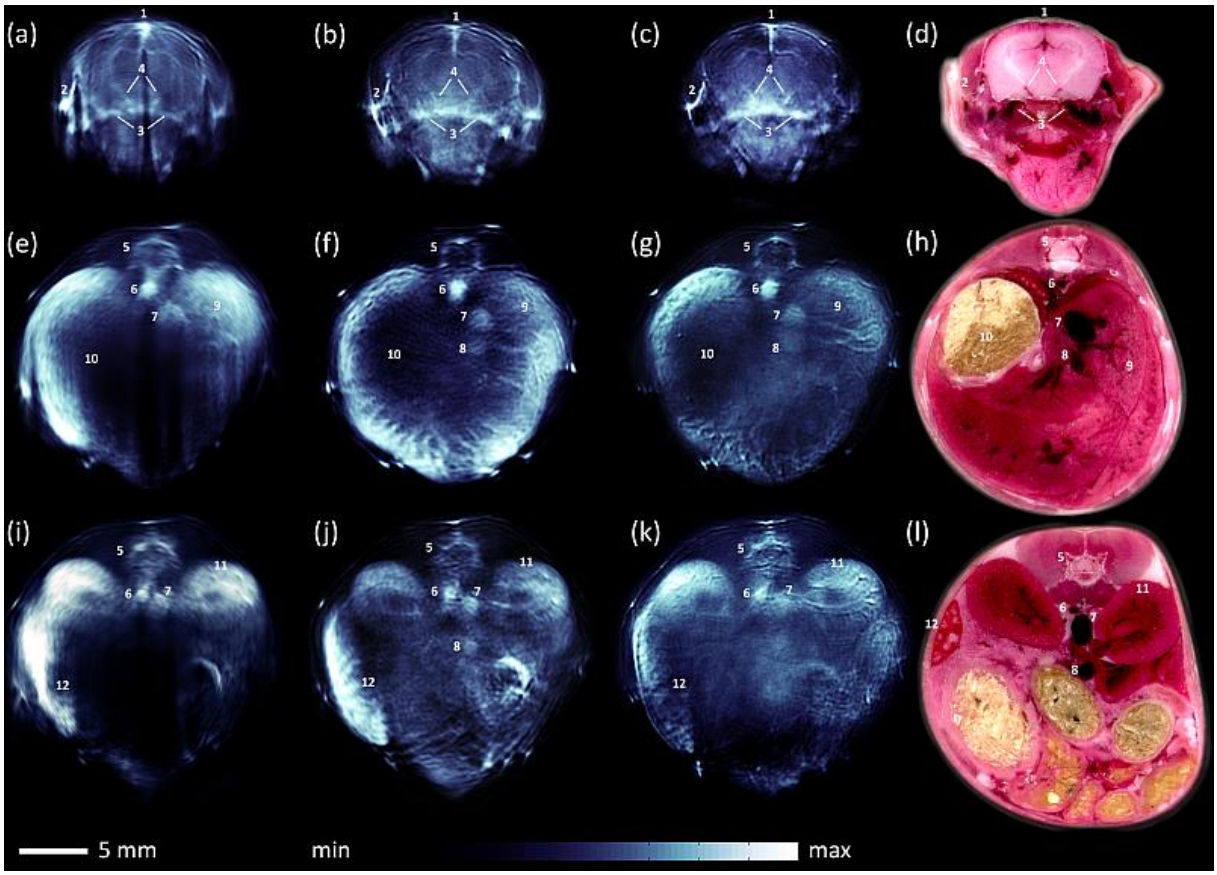

Fig. 6. Single-shot *in-vivo* mouse images at 900 nm wavelength: the first column shows results obtained from MSOT64; second column MSOT128; third column MSOT256. The last column shows mouse cryoslices at equivalent positions. The mouse head is shown in (a-d): 1. sagittal sinus; 2. temporal artery; 3. extra-cranial blood vessel; 4. deep cerebral vessel. The liver region is shown in (e-h): 5. spinal cord; 6. aorta; 7. vena cava; 8. vena porta; 9. liver; 10. stomach. The kidney region is shown in (i-l): 11. kidney; 12. spleen.

Analysis of the mouse head revealed that all transducer systems captured large vascular structures on the periphery as well as deep inside the brain. Compared to other body segments, the mouse head was covered reasonably well by all transducers, even by the small area sensitivity field of MSOT64, shown on Fig. 2. The temporal artery (marked 2), the sagittal sinus (marked 1) and deep seated extra-cranial (marked 3) and cerebral blood vessels (marked 4) were visible in all cases.

However, closer inspection of Fig. 6(a-d) reveals improving resolution for increasing number of detector elements. For example the sagittal sinus is only vaguely captured by MSOT64 with a transversal diameter of 600µm at its widest point, whereas it is more accurately reconstructed with MSOT128 (550µm diameter) and MSOT256 (450µm diameter). Similar inspection of the temporal artery revealed a reconstructed size of 670µm, 470µm and 380µm from MSOT64, MSOT128 and MSOT256 respectively. Comparison of the MSOT256 image and the cryoslice photograph on Fig. 6(d) shows that MSOT256 achieves the most accurate reconstruction of vessels over MSOT64 and MSOT128, offering an overall appearance that is very close to the one seen on the photograph.

MSOT results from the liver level are depicted in Fig. 6(e-h). MSOT64, shown in Fig. 6(e), allows localization of larger features, such as the spinal cord (marked 5), the aorta (marked 6) or the vena cava (marked 7). However several anatomical details in the periphery of the animal are lost, consistent with the findings in Fig. 4 and Fig. 5. Conversely, MSOT128, Fig. 6(f), and MSOT256, Fig. 6(g), reveal finer structures and more elaborate views of vasculature showing improved peripheral resolution and fewer artifacts.

Similar observations were obtained from images at the kidney region, where the diameter of the mouse body was about 23 mm. Fig. 6(i), obtained from MSOT64, exhibits resolution drop and visualization of coarse features, especially in the animal periphery as in Fig. 6(e) and affords only limited transversal resolution. Nonetheless, characteristic landmarks (spinal cord, aorta, vena cava) and large organs (both kidneys marked 11, spleen marked 12) can be identified. Fig. 6(j) depicts the MSOT128 result and shows better clarity in resolving anatomical features compared to MSOT64. As expected from the liver cross-section, the best image quality is achieved by MSOT256, depicted in Fig. 6(k). The significantly improved transversal resolution and sensitivity field is best demonstrated in the right kidney (marked 11).

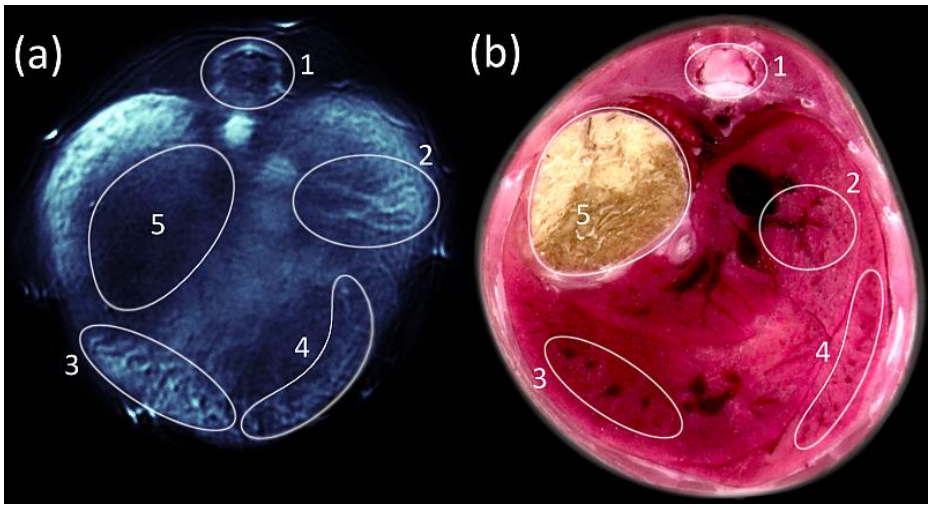

Fig. 7. Mouse cross-section at the liver level. (a) MSOT256 result *in-vivo* at 900 nm wavelength. (b) Equivalent cryoslice obtained from a similar mouse. Corresponding features have been encircled and numbered: 1. Spinal cord; 2-4. Vascular structures within the liver; 5. Stomach.

Due to its feature rich content, the liver region enables a detailed comparison of cryosection and MSOT images. Fig. 7 compares the performance of MSOT256 against a corresponding cryoslice photograph serving as the gold standard, to offer a more elaborate explanation of the signals observed on the optoacoustic images. Five significant landmarks have been encircled and numbered (1-5), whereby higher brightness in the MSOT image, Fig. 7(a), corresponds to darker colors in the cryosection, Fig. 7(b). The first landmark marks the vasculature surrounding the spinal disk; its structure comprises a bright dot at the center top, which is characteristic of a blood vessel perpendicular to the imaging plane, and a surrounding bracket indicating blood vessels in-plane. Landmarks 2-4 highlight different regions within the liver. Area 2 is dominated by elongated in-plane vasculature bifurcating from the vena cava and vena porta towards the periphery. On the other hand areas 3 and 4 contain vessels perpendicular to the imaging plane. The cryosection allows identification of 4-5 larger vessels in area 3 and >8 smaller vessels in area 4. Consequently the MSOT image indicates fewer but stronger dots in area 3 and more however weaker dots in area 4. Additionally, MSOT highlights short branches originating from the dots. These features can be

attributed to vascular branching close and perpendicular to the imaging plane. Finally, we also marked the stomach (area 5), because of its prominent position and sharp boundary.

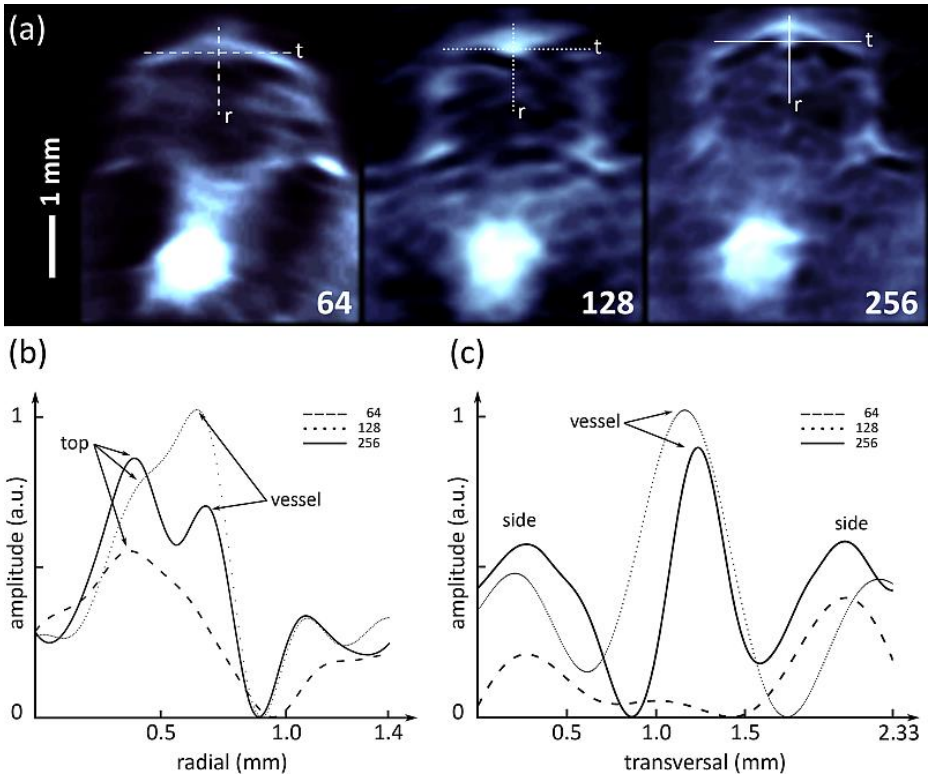

Fig. 8. Profiles of spinal cord at liver level. (a) Magnifications for MSOT64, MSOT128 and MSOT256. Cuts in radial (marked r) and transversal (marked t) direction are line-coded by array. (b) Profile of radial trace from top to bottom. (c) Profile of transversal trace from left to right. Prominent features: top and sides of in-plane vascular structure, blood vessel perpendicular to the imaging plane.

To better understand the relative *in-vivo* performance of the three systems employed, Fig. 8 offers a quantitative comparison between the reconstructions obtained by the 64, 128 and 256 element systems on the spinal disk. Image profiles taken from the radial and transversal directions (marked r and t) are highlighted on Fig. 8(a) as dashed (MSOT64), dotted (MSOT128) and solid (MSOT256); corresponding traces are shown in Fig. 8(b) and (c). A blood vessel perpendicular to the imaging plane was selected to mark the intersection point for orientation purposes. This vessel could be resolved with 128 and 256 elements, but not with 64 due to its close proximity to the top and

sides of the surrounding structure. The radial profile illustrates how the transversal resolution of the three systems can affect the result. In MSOT64, the vessel and the adjacent top edge are fused with emphasis given to the edge. In MSOT128 the vessel gives the stronger signal, however cannot be resolved from the edge. Finally only MSOT256 is able to clearly determine the distance between the two as 280µm (peak to peak). On the other hand, from the transversal profile the vessel diameter can be resolved as 560µm using MSOT128 and as 350µm with MSOT256. MSOT64 again cannot resolve the vessel due to a lack of sensitivity and transversal resolution.

4. Discussion

We studied the MSOT performance achieved in whole-body small animal imaging as a function of increasing number of detectors. Performance was studied numerically and experimentally on phantoms and animals *in-vivo*. The results highlighted improvements in resolution, region of interest, sensitivity and imaging artifacts with increasing angular coverage and detector density. An important finding was that the use of 256 elements yielded strong improvements over 128 elements, to justify deployment of high density arrays. Qualitatively, the in-vivo mouse images obtained using 256 elements showcased better resolution and image fidelity over those obtained using 64 or 128 elements, allowing the visualization of elaborate vascular patterns in the brain, spine, kidney or liver. In a controlled phantom measurement, we experimentally quantified the improvements. At the critical radius of 10 mm from the image center transversal resolution increased by a factor of 2.25 for 256 elements and 1.5 for 128 elements when compared to results from the 64 element system. Similarly, sensitivity at this radius improved for 128 elements by ~50% and ~150% for 256.

Besides higher resolution, an interesting feature identified in this study is that the field of view can be improved without sacrificing sensitivity when employing more transducers. Given the same azimuthal coverage, the 256 element array achieves a sensitivity field that is broader than the 128, which enables the use of larger animals. In [14] an array of even higher density was utilized,

however a significant number of averages was reported, which indicates low sensitivity. In contrast, images presented herein were obtained from a single laser pulse. Thus, when using comparable piezocomposite materials, array density should be chosen by element shape and area size relative to the system radius. Similarly, results from MSOT256 show that to obtain high quality images full view is not mandatory but can be reduced when choosing appropriate system radius and element size.

An additional inference however from these observations relates to quantification. As Fig. 2 shows, sensitivity drops significantly with increasing radius from the array center. Combined with possible inhomogeneity in illumination patterns, this can lead to quantification differences for objects placed at different areas in the imaging plane. Using the study performed herein, such inhomogeneity can be well characterized, in particular detector sensitivity which is an implicit characteristic of element and array geometry. The sensitivity field of each transducer needs therefore characterization and implementation in the inversion code to achieve correct quantitation across the imaging plane.

For many biological applications the use of MSOT64 can be regarded sufficient as it provides still a marked improvement over two-dimensional optical imaging systems or tomographic implementations which attain 10 times worse resolution. However with the documented higher transversal resolution and image quality established by the MSOT128 or the MSOT256, these systems offer superior performance and should be preferred for achieving an all-around better imaging quality. With the MSOT256 yielding the larger field of view (FWHM sensitivity field) and resolution of the three systems studied, scanning of larger animals or the use of more challenging animal models becomes interesting.

Nonetheless challenges remain. While a 2D image is derived from a consistent, motion-free dataset, the full-body scan, i.e. the 3D dataset, cannot be acquired in real time. Improvements in laser repetition rates and continuous translation implements could lead to fast 3D scans with the geometrical implementations considered herein. Since it is unlikely that truly real-time 3D systems

can be widely disseminated, as they would come at a very high cost, 2D curved array systems will possibly remain a reasonable option not only for 2D imaging but also for 3D scans.

[1] J. S. Lewis, S. Achilefu, J. R. Garbow *et al.*, "Small animal imaging: current technology and perspectives for oncological imaging," *European Journal of Cancer,* vol. 38, no. 16, pp. 2173-2188, 2002.

[2] R. A. de Kemp, F. H. Epstein, C. Catana *et al.*, "Small-Animal Molecular Imaging Methods," *Journal of Nuclear Medicine,* vol. 51, no. Supplement 1, pp. 18S-32S, May 1, 2010, 2010.

[3] V. Ntziachristos, "Going deeper than microscopy: the optical imaging frontier in biology," *Nat Meth,* vol. 7, no. 8, pp. 603-614, 2010.

[4] A. Rosencwaig, and P. R. Griffiths, "Photoacoustics and Photoacoustic Spectroscopy," *Physics Today,* vol. 34, no. 6, pp. 64-66, 1981.

[5] R. A. Kruger, "Photoacoustic ultrasound (PAUS)—Reconstruction tomography," *Medical Physics,* vol. 22, no. 10, pp. 1605-9, 1995.

[6] A. Taruttis, M. Wildgruber, K. Kosanke *et al.*, "Multispectral optoacoustic tomography of myocardial infarction," *Photoacoustics,* vol. 1, no. 1, pp. 3-8, 2013.

[7] D. Razansky, C. Vinegoni, and V. Ntziachristos, "Multispectral photoacoustic imaging of fluorochromes in small animals," *Optics Letters,* vol. 32, no. 19, pp. 2891-2893, 2007.

[8] X. Wang, Y. Pang, G. Ku *et al.*, "Noninvasive laser-induced photoacoustic tomography for structural and functional in vivo imaging of the brain," *Nature Biotechnology,* vol. 21, no. 7, pp. 803-806, 2003.

[9] R. Ma, A. Taruttis, V. Ntziachristos *et al.*, "Multispectral optoacoustic tomography (MSOT) scanner for whole-body small animal imaging," *Opt. Express,* vol. 17, no. 24, pp. 21414-21426, 2009.

[10] E. Z. Zhang, and et al., "In vivo high-resolution 3D photoacoustic imaging of superficial vascular anatomy," *Physics in Medicine and Biology,* vol. 54, no. 4, pp. 1035, 2009.

[11] V. Kozhushko, T. Khokhlova, A. Zharinov *et al.*, "Focused array transducer for two-dimensional optoacoustic tomography," *The Journal of the Acoustical Society of America,* vol. 116, no. 3, pp. 1498-1506, 2004.

[12] H.-P. Brecht, R. Su, M. Fronheiser *et al.*, "Whole-body three-dimensional optoacoustic tomography system for small animals," *Journal of Biomedical Optics,* vol. 14, no. 6, pp. 064007-8, 2009.

[13] L. Song, K. Maslov, R. Bitton *et al.*, "Fast 3-D dark-field reflection-mode photoacoustic microscopy in vivo with a 30-MHz ultrasound linear array," *Journal of Biomedical Optics,* vol. 13, no. 5, pp. 054028-5, 2008.

[14] J. Xia, M. R. Chatni, K. Maslov *et al.*, "Whole-body ring-shaped confocal photoacoustic computed tomography of small animals in vivo," *Journal of Biomedical Optics,* vol. 17, no. 5, pp. 050506-1, 2012.

[15] R. A. Kruger, R. B. Lam, D. R. Reinecke *et al.*, "Photoacoustic angiography of the breast," *Medical Physics,* vol. 37, no. 11, pp. 6096-6100, 2010.

[16] A. Bühler, X. L. Deán-Ben, J. Claussen *et al.*, "Three-dimensional optoacoustic tomography at video rate," *Optics Express,* vol. 20, no. 20, pp. 22712-22719, 2012.

[17] L. Xiang, B. Wang, L. Ji *et al.*, "4-D Photoacoustic Tomography," *Sci. Rep.,* vol. 3, 2013.

[18] A. Buehler, E. Herzog, D. Razansky *et al.*, "Video rate optoacoustic tomography of mouse kidney perfusion," *Optics Letters,* vol. 35, no. 14, pp. 2475-2477, 2010.

[19] A. Buehler, M. Kacprowicz, A. Taruttis *et al.*, "Real-time handheld multispectral optoacoustic imaging," *Optics Letters,* vol. 38, no. 9, pp. 1404-1406, 2013.

[20] A. Taruttis, S. Morscher, N. C. Burton *et al.*, "Fast Multispectral Optoacoustic Tomography (MSOT) for Dynamic Imaging of Pharmacokinetics and Biodistribution in Multiple Organs," *Plos One,* vol. 7, no. 1, pp. e30491, 2012.

[21] N. C. Burton, M. Patel, S. Morscher *et al.*, "Multispectral Opto-Acoustic Tomography (MSOT) of the brain and glioblastoma characterization," *Neuroimage,* vol. 15, no. 65, pp. 522-528, 2012.

[22] E. Herzog, A. Taruttis, N. Beziere *et al.*, "Optical Imaging of Cancer Heterogeneity with Multispectral Optoacoustic Tomography," *Radiology,* vol. 263, no. 2, pp. 461-468, May 1, 2012, 2012.

[23] A. Dima, and V. Ntziachristos, "Non-invasive carotid imaging using optoacoustic tomography," *Optics Express,* vol. 20, no. 22, pp. 25044-25057, 2012.

[24] D. Razansky, A. Buehler, and V. Ntziachristos, "Volumetric real-time multispectral optoacoustic tomography of biomarkers," *Nat. Protocols,* vol. 6, no. 8, pp. 1121-1129, 2011.

[25] A. Rosenthal, D. Razansky, and V. Ntziachristos, "Fast semi-analytical model-based acoustic inversion for quantitative optoacoustic tomography," *IEEE Transactions on Medical Imaging,* vol. 29, no. 6, pp. 1275-1285, 2010.

[26] J. A. Jensen, "Field: A Program for Simulating Ultrasound Systems," *Medical & Biological Engineering & Computing,* vol. 34, no. Supplement 1, Part 1, pp. 351-353, 1996.

[27] J.A. Jensen, and N. B. Svendsen, "Calculation of pressure fields from arbitrarily shaped, apodized and excited ultrasound transducers," *Ieee Transactions on Ultrasonics Ferroelectrics and Frequency Control,* vol. 39, pp. 262-267, 1992.

[28] G. J. Diebold, and P. J. Westervelt, "The photoacoustic effect generated by a spherical droplet in a fluid," *Journal of the Acoustical Society of America,* vol. 84, no. 6, pp. 2245-2251, 1988.